

Magnetic and electric responses from artificial nanocomposites

Reza Gholipur¹ · Ali Bahari¹

Received: 3 December 2015 / Accepted: 15 April 2016 / Published online: 27 April 2016
© Springer-Verlag Berlin Heidelberg 2016

Abstract Random silver nanowires embedded in Ni-doped zirconia ($Zr_{0.9}Ni_{0.1}O_y$) dielectric were prepared by co-precipitation technique. The morphology and structure properties of $Ag/Zr_{0.9}Ni_{0.1}O_y$ (AZNx; where “x” is $[Ag]/[Zr_{0.9}Ni_{0.1}O_y] = x$) nanocomposites were studied by X-ray diffraction, scanning electron microscopy, atomic force microscopy, transmission electron microscopy, and X-ray photoelectron spectroscopy techniques. Interesting negative permittivity and permeability behaviors of AZNx are found. The experimental data of the negative permittivity are fitted well by Drude model. These results have important implications for the realization of double-negative properties in AZNx as a promising candidate for the double-negative materials.

1 Introduction

The topic of metamaterials, as specially engineered media, has received ever increasing attention in recent years [1, 2]. Media in which one or both of the material parameters, permittivity (ϵ) and permeability (μ), can attain negative real parts in a certain frequency band, have been the subject of study by numerous groups [3–27]. When both material parameters possess negative real parts, such media are called as DNMs, while media with a single-negative parameter are called as single-negative (SNG) media.

It has been proposed that electromagnetic metamaterials composite formed either from periodic or random arrays of

scattering elements should respond to electromagnetic radiation as continuous materials [28, 29].

Random metal-dielectric composites, such as nano-caled semicontinuous metallic structures, exhibit optical and electrical transport properties that are notably different from those of their corresponding bulk counterparts [30–40].

The use of metal-dielectric composite is an interesting route to obtain materials with tailorable dielectric and permeability functions. In particular, random metal-dielectric composites are easy to prepare using thin-film deposition techniques and their effective dielectric function can be varied by controlling the mixture composition and particle shape [41]. The performance of metal-dielectric multilayer subwavelength imaging structures can be improved when replacing the metal layers by metal-dielectric composites [42, 43]. These composites may enable wavelength tuning of super-resolution devices [44], improve the performance of negative index structures [45, 46], cloaking devices [25], and provide transparency or extreme anisotropy [47].

The electromagnetic responses of a material are determined by two parameters: ϵ and μ . The negative index metamaterial, for which both the electric permittivity and the magnetic permeability are simultaneously negative, relied on an earlier theoretical prediction that an array of nonmagnetic conductive elements could exhibit a strong, resonant response to the magnetic component of an electromagnetic field [29]. A negative permittivity is not unusual and occurs in any metal from zero frequency to the plasma frequency (ω_p). The plasma oscillation of conduction electrons provided by metal inclusion will be evoked for near percolation threshold (p_c) and negative permittivity appears. This implies that the concentration of electrons play a significant role. The techniques applied in those

✉ Ali Bahari
bahari.pa.a@gmail.com

¹ Department of Solid State Physics, University of Mazandaran, Babolsar 4741695447, Iran

studies probed the materials indirectly and did not provide an explicit measurement that would assign values for ϵ and μ .

For random metamaterials, several homogenization approaches are that cover a wide range of methods and approximations, including a variety of field-averaging approaches, the curve-fitting approach, a dispersion-equation method, and the scattering parameter extraction method [6, 48, 49]. The response of a metamaterial to an electromagnetic field is dependent on the specific architecture of the meta-atoms.

In the present work, we experimentally show that Ag metal nanowires embedded randomly in a $Zr_{0.9}Ni_{0.1}O_y$ dielectric medium can exhibit negative permittivity and permeability at ~ 7.5 – 10 GHz frequencies. For metamaterials at microwave to infrared frequencies, silver is the metal of choice mainly because of its superior (smaller) loss factor compared. Moreover, a material with a relatively large dielectric constant is favored for the host dielectric. Therefore, in the present structure, Ni-doped zirconia is used.

2 Experimental

2.1 Dielectric synthesis

The $Zr_{0.9}Ni_{0.1}O_y$ nanostructural sample was prepared through co-precipitation technique using NH_4OH solution. Zirconyl chloride octahydrate [$ZrOCl_2 \cdot 8H_2O$] and nickel(II) chloride [$NiCl_2 \cdot 6H_2O$] were used as the dielectric precursors. Aqueous solutions of 1 M concentrations of zirconyl chloride octahydrate and nickel(II) chloride were prepared. NH_4OH solution was added dropwise to a beaker containing solution with 90 wt% zirconyl chloride octahydrate and 10 wt% nickel(II) chloride stirring by a magnetic stirrer.

2.2 Silver nanoparticles growth

Silver nanoparticles were synthesized by reducing $AgNO_3$ in a polyol such as ethylene glycol (EG) [$C_2H_6O_2$]. Polyvinyl pyrrolidone (PVP) was introduced as a structure-directing agent. Gold nanoparticles derived by in situ pre-reducing chloroauric acid ($HAuCl_4$) in ethylene glycol were used as seeds. Firstly, $HAuCl_4$ solution was prepared from mixing of 10 mL of EG with 1 mL of 0.005 M $HAuCl_4$. A few minutes later, 170 mg of $AgNO_3$ dissolved in 10 mL of EG and 170 mg of PVP dissolved in 10 mL of EG were added into $HAuCl_4$ solution with the same injection rate of 2 mL/min. This solution was stirred vigorously at 160 °C for 2 h. Silver nanowires began forming at this stage.

The solution was diluted with acetone and centrifuged at 2000 rpm for ~ 20 min. Ag nanoparticles were dispersed in Zr and Ni solution with different atomic ratios “ x ” (where “ x ” is 0, 0.05, and 0.15) under vigorous magnetic stirring. The solution was poured into a plastic dish and sonicated for 60 min. The sample was dried at 80 °C for 24 h.

2.3 Analyses of phase and morphology

For the crystal and phase analyses, XRD measurements with $Cu K\alpha$ ($\lambda = 1.5408 \text{ \AA}$) radiation by GBC-MMA007 (2000) were taken. Microscopy analysis and surface morphology were performed using SEM, AFM, and TEM techniques. The SEM, TEM, and AFM images of the films were studied by XL30-PHILIPS, CM10-PHILIPS, and LIQUID Flex AFM, respectively. The AFM images were analyzed using the DME-SPM software.

2.4 The permittivity and permeability measurements

The theories for the permittivity and permeability measurements are “parallel plate capacitor” and “inductance” methods. The parallel plate capacitor method involves sandwiching material between two electrodes to form a capacitor. The inductance method derives the permeability by measuring the inductance of the material. The concept is to wind some wire around material under test and evaluate the inductance with respect to the ends of the wire. The permittivity and permeability as functions of frequency were measured using test fixtures (Fig. 1) and GSP-730 analyzer [2]. The test fixtures consist of material characterized by a permittivity and a permeability denoted by $\epsilon_e = \epsilon'_e + i\epsilon''_e$ and $\mu_e = \mu'_e + i\mu''_e$, respectively. The real and imaginative parts of permittivity and complex permeability were determined from the following formulas [50],

$$\epsilon'_e = \frac{Cl}{\epsilon_0 A} \quad (1)$$

$$\epsilon''_e = \frac{l}{RA\omega\epsilon_0} \quad (2)$$

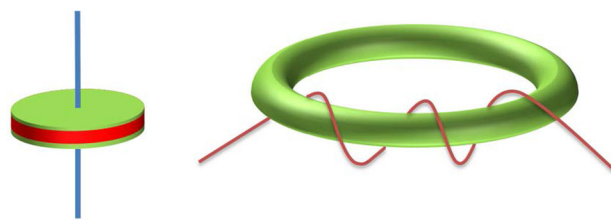


Fig. 1 The circular disk (12 mm \times 2 mm; diameter a and thickness l) and toroidal test fixtures (6.5 mm \times 19 mm \times 2 mm; inner diameter c , outer diameter d and height h)

$$\mu_e = \frac{2\pi(L - L_0)}{\mu_0 h \ln \frac{d}{c}} + 1 \tag{3}$$

$$L = \frac{Z^*}{i\omega} \tag{4}$$

where l is the sample thickness, C the capacitance, R the resistance, A the electrode plate area, ϵ_0 the absolute permittivity of free space, L and L_0 are the self-inductance of toroidal test fixture with and without sample, Z^* is the complex impedance of toroidal test fixture with sample, ω is the frequency, and μ_0 is the space permeability.

3 Results and discussion

3.1 XPS

The surface chemical compositions and chemical states of the products are investigated using XPS. XPS technique is a quantitative technique in the sense that the number of electrons recorded for a given transition is proportional to the number of atoms at the surface. The typical XPS survey spectrum of AZN0.15 nanostructures is presented in Fig. 2. As can be seen, sample contains Ag, Zr, Ni, and O elements. The XPS spectrum reveals that the Ag 4*d*, Ag 4*p*, Ag 4*s*, Zr⁴⁺ 3*d*, Ag 3*d*, O 1*s*, and Ni³⁺ 2*p* peaks have binding energy centered at 5.8, 59.6, 97.7, 188.2, 368.6, 534.4, and 856.4 eV, respectively. In addition, the XPS peak for C 1*s* at binding energy of 288.3 eV (assigned to aliphatic carbon set) is ascribed to the adventitious carbon from the XPS instrument.

3.2 XRD and size measurement

Figure 3 shows the XRD patterns of AZN_x samples. The XRD data indicated the presence of a two-phase mixture of monoclinic phase of Ag and tetragonal phase of Zr_{0.9}Ni_{0.1}O_y.

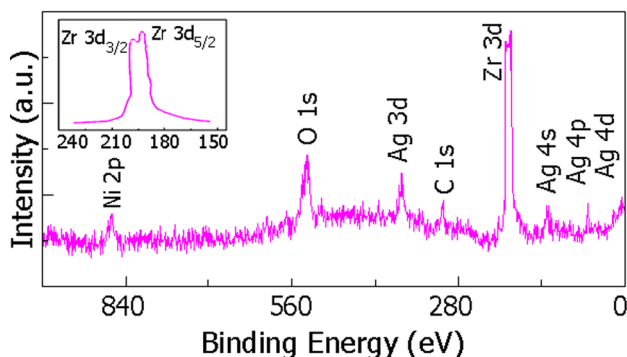


Fig. 2 XPS spectra of AZN0.15 sample showing characteristic peaks of Ag, Zr, Ni, O, and C. The inset in the figure represents the Zr⁴⁺ 3*d*_{3/2}, Zr⁴⁺ 3*d*_{5/2}

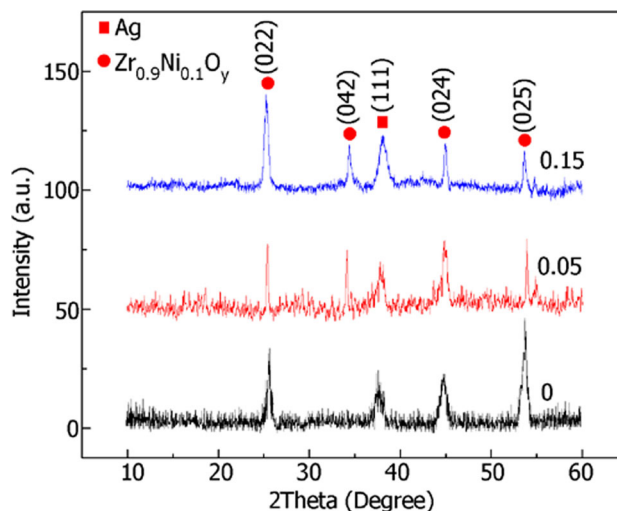


Fig. 3 XRD patterns of the AZN_x samples ($x = 0, 0.05, \text{ and } 0.15$)

It was also found that as the molar silver content increased, the width of the peaks became stronger. Furthermore, the intensities of different diffraction peaks are different, which indicates that the growth of AZN_x in various planes is different and the growth is anisotropic.

From Fig. 3, it is also observed that for AZN0.15, there is high intensity of peaks, predominantly (022), (042), (024), and (025) with high full width at half maximum (FWHM). This suggests good crystalline quality of AZN0 sample.

The five main diffraction peaks of Zr_{0.9}Ni_{0.1}O_y and Ag identified with the JCPDS databases (01-081-0610) and (00-001-1164), respectively, are typical of this phase. Moreover, the shift of the (042) diffraction peak toward the higher angles is observed when the Ag content increases. The peak corresponds to the cubic silver of AZN0.15, with a lattice constant of $a = 4.001 \text{ \AA}$, which is in agreement with the reported values $a = 4.079 \text{ \AA}$ (JCPDS 00-001-1164).

From XRD spectra, the crystallite size (D) of AZN_x films was obtained using the Debye–Scherrer formula, shown in Eq. (5) [51]:

$$D = \frac{0.94\lambda}{\beta \cos \theta} \tag{5}$$

where $\lambda = 1.5408 \text{ \AA}$ and β is the FWHM.

It was calculated that as the molar silver content increased, the average crystallite size of the Ag nanoparticles became smaller.

Table 1 is the result of the analysis of the diffractogram of the samples with reference to the ICDD standard. The 2θ of the samples diffractogram was evaluated with that of the standard. The difference in the values of the 2θ for the samples and the standard was found to be ≤ 2 which can still be considered to be within the range.

Table 1 The 2θ angle, d -space, Miller indices, and grain size of AZNx

Sample	2θ ICDD standard	2θ analyzed sample	d -spacing (\AA) analyzed sample	Size (nm)	Miller indices (h k l)
$x = 0$	25.982	25.98	3.42	62	(022)
	38.600	38.34	2.34	57	(042)
	44.509	44.88	2.01	43	(024)
	54.984	54.22	1.69	61	(025)
$x = 0.05$	25.982	24.7	3.59	66	(022)
	37.934	38.77	2.32	25	(111)
	38.600	34.91	2.56	66	(042)
	44.509	45.01	2.01	55	(024)
$x = 0.15$	54.984	54.88	1.67	66	(025)
	25.982	24.71	3.59	62	(022)
	37.934	38.82	2.31	22	(111)
	38.600	34.94	2.56	62	(042)
	44.509	45.01	2.01	62	(024)
	54.984	54.86	1.67	62	(025)

3.3 Morphology analyses

The morphology of AZNx samples was observed by SEM images (Fig. 4). Figure 4a shows nanosized grain structure of AZN0. As Fig. 4a shows, no nanowire was obtained when there is no silver. It was found that the AZN0 reveals wide edges and corners with spherical shapes of fine nanostructure, fine-grained, and dense film surface with an average grain size of 70–180 nm, which is much bigger as compared to the structure sizes observed in the AZN0.15 sample. Figure 4b shows randomly oriented and distinct prolate spheroid structures. Figure 4b shows the grains with prolate spheroid shapes with length of about 20–300 nm and diameters of 2–20 nm. As the silver molar content increases, the grains become uniform prolate spheroid structures (nanowires) with length of about 1000–1700 nm and diameters of 10–20 nm (Fig. 4c). Figure 4c shows the sample surface increases the random distribution of nanowires, coarseness, and in homogeneity with increasing Ag doping. This is understandable from the fact that Ag plays a key role in the growth of the nanowires. The aspect ratio is on the order of ~ 50 .

The AFM images of AZNx samples are shown in Fig. 5. The morphology of AZN0 sample is shown in Fig. 5a. Particles are several nanometers in diameter (~ 100 nm), appear bundled together. Figure 5a reveals this bundling (lengthwise aggregation) and also shows the structures to be many sided rather than smooth wires. This confirms previous results of the SEM images. It is observed that the particle size of AZN0 is decreased with the increase in Ag-doping level. Figure 5a shows the surface roughness of the AZN0 change with the increase in Ag-doping level from 0 to 0.15. As the silver molar content increases to 0.05, the nanoparticle can be seen interspersed with the irregularly large-shaped particles, and the size of particles was fairly

uniform (Fig. 5b). The AFM image in Fig. 5c shows silver nanowires, which are about 1 μm long and 20 nm wide. These stable nanowires grow specifically along one given direction. All surfaces showed good homogeneity with no surface cracks. AZN0.15 sample is seen to be polycrystalline in nature, with no significant difference in nanowires size. As shown in this figure, semicontinuous and irregular films were formed, with significant changes in morphology. The root-mean-square (RMS) of the AZN0, AZN0.05, and AZN0.15 was measured by AFM over the area of $1 \times 1 \mu\text{m}^2$ which are 0.27, 0.51, and 0.5 nm, respectively.

Figure 6 shows TEM images of AZN0.15 nanowires before processing and after processing. Figure 6a gives a TEM image of AZN0.15 sample that were wired-like in shapes with an average diameter of ~ 18 nm. The wired-like branches of elongated spheroid particle of Ag lead to the formation of the network. The TEM image is evidence in support of the explanation for the formation mechanism of the wired-like network structure of Ag. The PVP molecules play a key role in the formation of such a wired-like network structure of Ag and mainly act as the structure-directing agent of Ag. The wired-like network can be because of production of $[\text{Ag}(\text{PVP})]^+$ ions and then wiring process. Firstly, Ag^+ ions are connected to the PVP molecule. With reduction of Ag^+ ions and homogeneous nucleation process, the grains form. Wires of Ag grains may form under the effect of the polymeric PVP ligand. A primary purpose of the introducing PVP was to protect Ag nanoparticles from growing and agglomerating. This confirms the nearly free growth of the nanowires.

Figure 6b is image after converting to the respective binary black-white images. The black-white image corresponding to TEM image was then used to compute the filling fraction. The filling fraction of the composite is about 15 %.

Fig. 4 SEM images of: **a** AZN0; **b** AZN0.05; **c** AZN0.15 samples

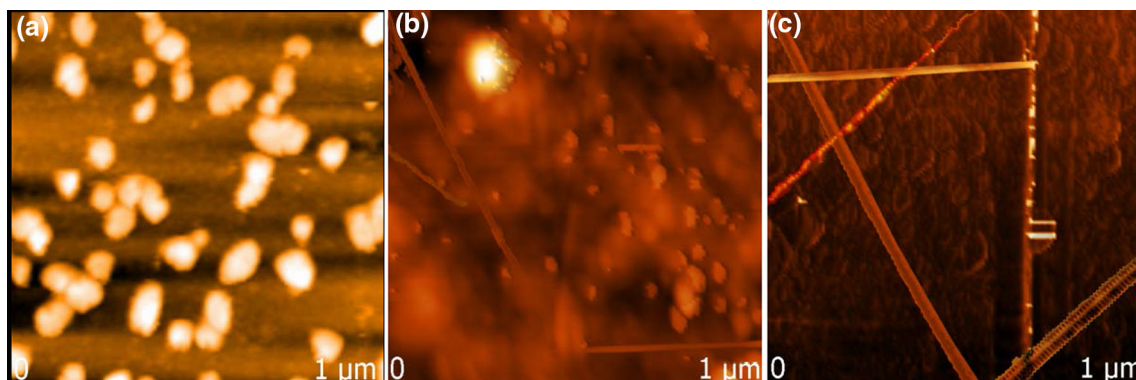
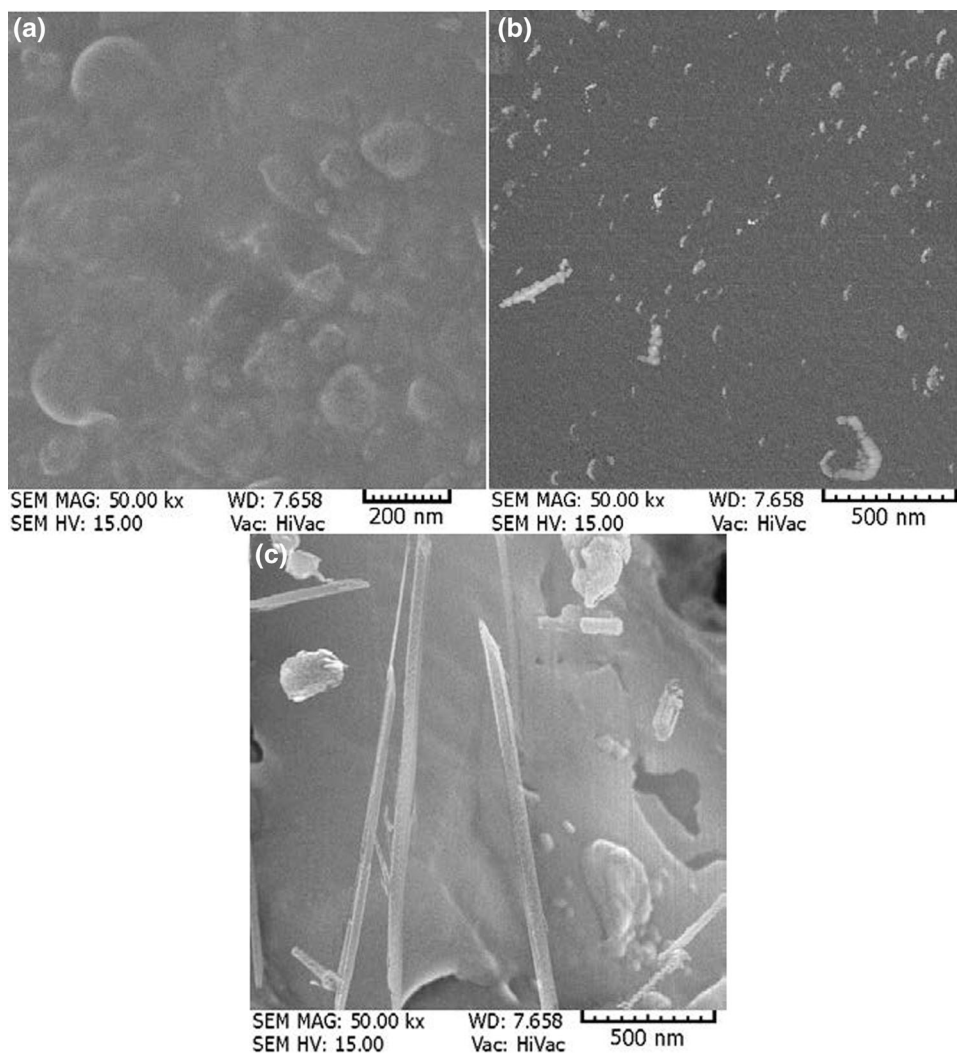


Fig. 5 AFM topography 2D images of **a** AZN0; **b** AZN0.05; **c** AZN0.15 samples

3.4 The permittivity and permeability analyses

The real parts of the effective dielectric constant (ϵ'_e) of AZN_x nanocomposites are shown in Fig. 7a, b.

The real part of ϵ_e for AZN0 decreases with frequency slowly. ϵ'_e is positive and decreases with increasing frequency because of polarizations of localized electrons and interfacial. Moreover, ϵ'_e increases with higher silver content

Fig. 6 TEM image of AZN0.15 sample **a** before processing; **b** after processing

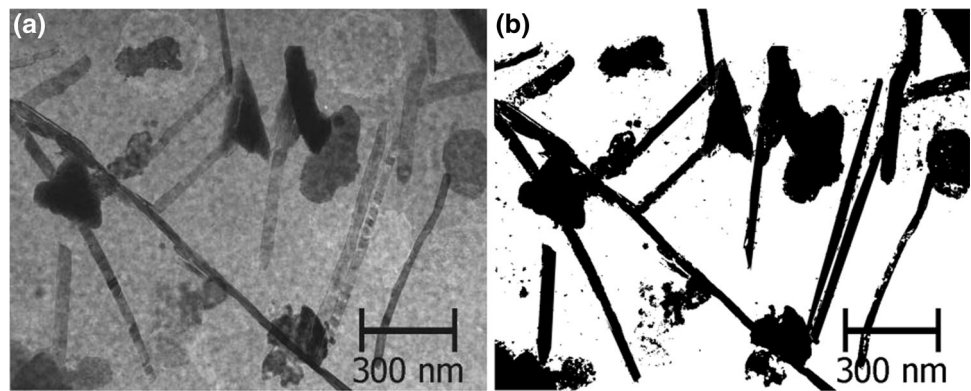
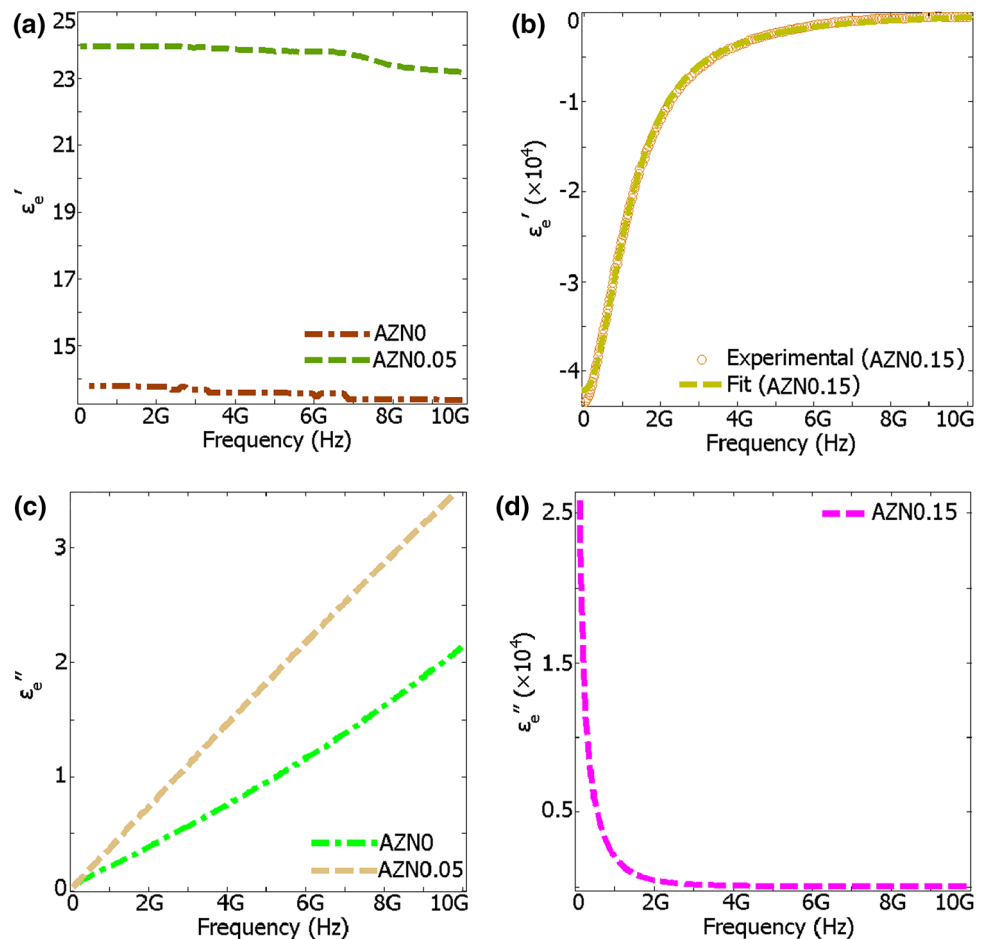


Fig. 7 Frequency dependence of **a** and **b** real parts and fitted results; **c** and **d** imaginary parts of the effective dielectric constant for AZNx samples



because of the increase of Ag–Zr_{0.9}Ni_{0.1}O_y interface area. By increasing the Ag content, the effect of Ag particles on the dielectric behavior of the composites becomes remarkable. Interestingly, the ϵ'_e turns negative when the silver content reaches 15 wt% (above p_c). The negative ϵ'_e implies the absence of polarization generated by dielectric.

The behavior of the ϵ'_e of AZN0.15 sample is well fitted by the frequency dispersion formula of modified Drude theory as follows:

$$\epsilon'_e = 1.00 - \frac{301.7}{\left(4759 \times \left(\frac{\nu}{1\text{E}12}\right)^2 + \frac{50.02}{7\text{E}3}\right)}; \quad \text{for AZN0.15} \quad (6)$$

where ν is frequency. For AZN0.15 sample, the ϵ'_e has metallic-like behavior and its sign is negative when $\omega < \text{plasma frequency } (\omega_p)$. According to formula (6), ω_p are damping constant and (Γ) are about 1.581 THz and

7.695 GHz, respectively. This equation gives a dispersion behavior of the effective dielectric constant ϵ_e' .

Figure 7c, d presents the dependence of the imaginary parts of the effective dielectric constant (ϵ_e'') of the AZNx samples on frequency. As shown in Fig. 7c, d, ϵ_e'' is dependent of the whole measured frequency range for the AZNx samples. As for the AZN0 and AZN0.05 samples (below p_c), ϵ_e'' shows a slight slope with increasing frequency because of increasing dielectric loss and leakage conductance loss. When Ag content reaches the value of 0.15 (above p_c), ϵ_e'' reduces rapidly with frequency, e.g., from 0.5 to 1 GHz.

Figure 8a shows the frequency dependence of real parts of the effective permeability (μ_e') for AZNx samples. The encapsulation of Ag nanowires with $Zr_{0.9}Ni_{0.1}O_y$ results in the enhancement of magnetic property resulting from the $Zr_{0.9}Ni_{0.1}O_y$ magnetic resonance and increased inductance and capacitance. There is no detection of relaxation and resonance peak in the test range. It is worth pointing out that the μ_e' of AZN0.15 is smaller than the μ_e' of AZN0.05 sample, which can be attributed to the topology of AZN0.15 sample. It is clear that AZN0.15 sample as the geometry of randomly oriented nanowires has caused a rise of low inductance and capacitance and hence a decline in magnetic response in the test frequency ranges inside the AZN0.15 composite. Hence, the μ_e' can be considered low in the frequency range.

In the high frequency range, because of eddy currents and Lenz's law, the real part of the magnetic permeability becomes smaller than zero, and diamagnetic behavior for AZN0.15 sample appears near the frequency of 7.5 GHz.

The domain wall motion and gyromagnetic spin resonances of dielectric medium contribute to the negative μ_e' phenomenon and continuous decrease of μ_e' with increasing frequency. The AZN0.15 sample has negative response at some frequencies. The reason for such behavior is the collective response of the wired-like network structure and dielectric medium to the electromagnetic field. The wired-

like network structure forms various closed circuits in the sample. The external magnetic field excites electric currents in these closed circuits. Magnetic moments of the currents flowing in the closed circuits and dielectric medium are in charge for the magnetic response of the AZN0.15 sample. The extra electromagnetic field induced by the current loops will be opposite to the external high-frequency electromagnetic field. Once the strong electromagnetic field induced by the current loops cancels or dominates the external magnetic field, the negative permeability behavior may occur.

Plots of imaginary parts of the effective magnetic permeability (μ_e'') versus frequency for the AZNx samples are shown in Fig. 8b. The μ_e'' decreases in the high frequency range as the Ag content increases. The frequency at the maximum of the μ_e'' decreases on approach to the 5 wt% Ag.

In the case of percolation systems containing conducting particles of elongated shape, the value of the percolation threshold concentration p_c can decrease with an increase in the aspect ratio of the inclusions and can generally be small. However, above the percolation threshold the values of the effective magnetic permeability depend on aspect ratio. Clearly, when the concentration is appropriate in a system of nonconducting particles, the effective magnetic properties may vanish practically completely. Therefore, the effective magnetic properties of composite systems with low values of p_c can only be because of the formation of anomalously large percolation clusters.

3.5 Electrical analyses

The frequency responses of reactance Z'' for AZNx samples are shown in Fig. 9. It can be seen that for the AZN0 and AZN0.05 samples, the signs of reactance are negative, which manifests capacitive character, and for the AZN0.15 sample, the sign of reactance is positive, which manifest inductive character.

Fig. 8 Plots of **a** real parts; **b** imaginary parts of the effective magnetic permeability for AZNx samples

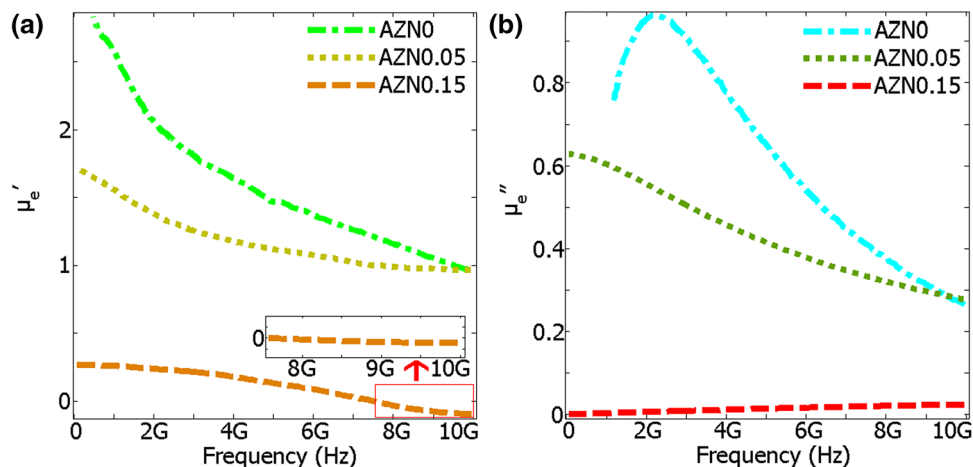


Fig. 9 Frequency dependence of reactance for AZN x samples **a** $x = 0$ and 0.05; **b** $x = 0.15$

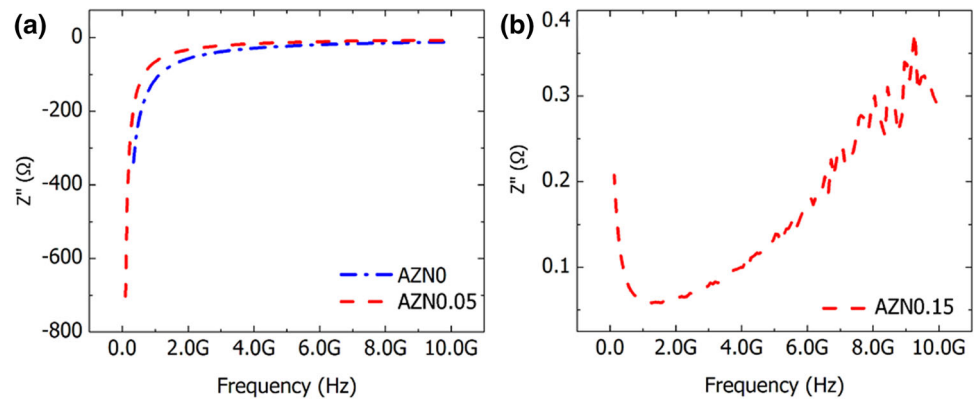


Fig. 10 Frequency dispersions of ac conductivity for AZN x samples **a** $x = 0$ and 0.05; **b** $x = 0.15$

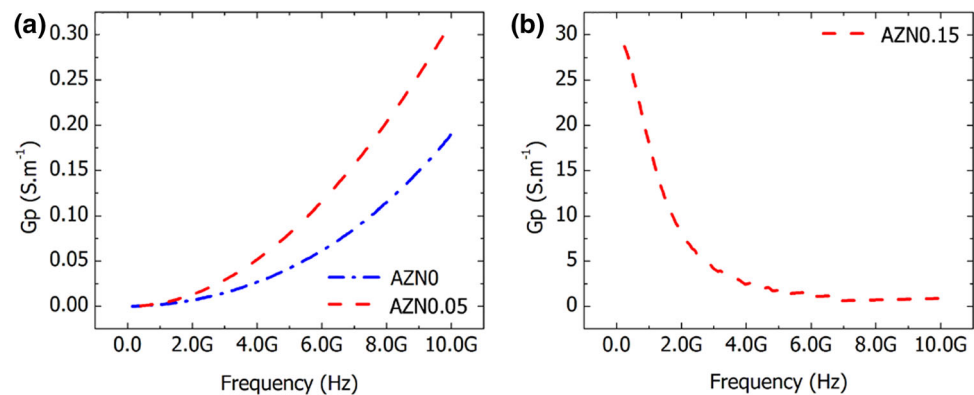
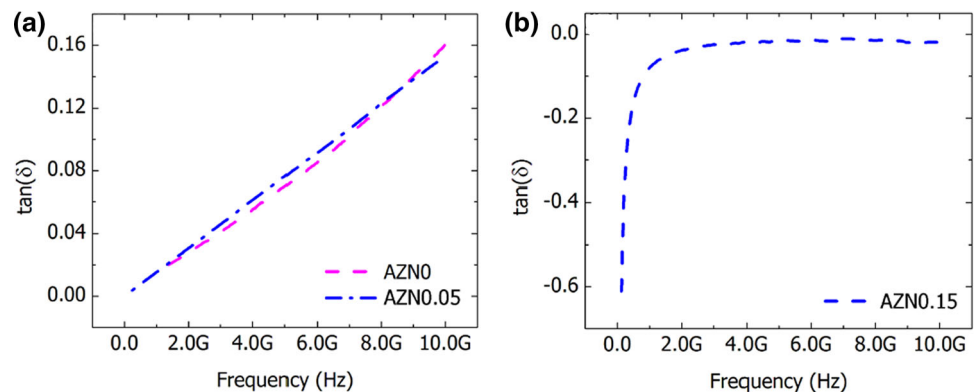


Fig. 11 Frequency dependence of loss tangent for AZN x samples **a** $x = 0$ and 0.05; **b** $x = 0.15$



The frequency dependence of ac conductivity (G_p) for AZN x samples is shown in Fig. 10. As shown in Fig. 10, higher silver content results in the increase of G_p due to the enhanced interconnection of silver particles.

The G_p of the AZN0 and AZN0.05 samples (Fig. 10a) increases with frequency because of their capacitive behavior. For AZN0.15 sample (Fig. 10b), G_p decreases with frequency because of its inductive behavior and the skin effect of delocalized electrons in interconnected silver particles.

In Fig. 11, the loss tangent is plotted against frequency for AZN x samples. The dielectric loss ability is gradually

enhanced with increasing Ag content (Fig. 11a). The values of $\tan(\delta)$ for AZN0.15 sample (Fig. 11b) are negative values indicating that the AZN0.15 sample has reflexive property.

As is well known, equivalent circuit models can be used to more directly analyze the electrical properties of percolative materials. We can describe each metal wire or cluster as an inductance L connected in series to a resistance R . The dielectric gaps, in turn, act as capacitive elements and are represented by a capacitance C . Hence, composite samples can be viewed as a network of RLC circuits.

Fig. 12 Equivalent circuit analysis of the AZN_x samples **a** AZN0; **b** AZN0.05; **c** AZN0.15

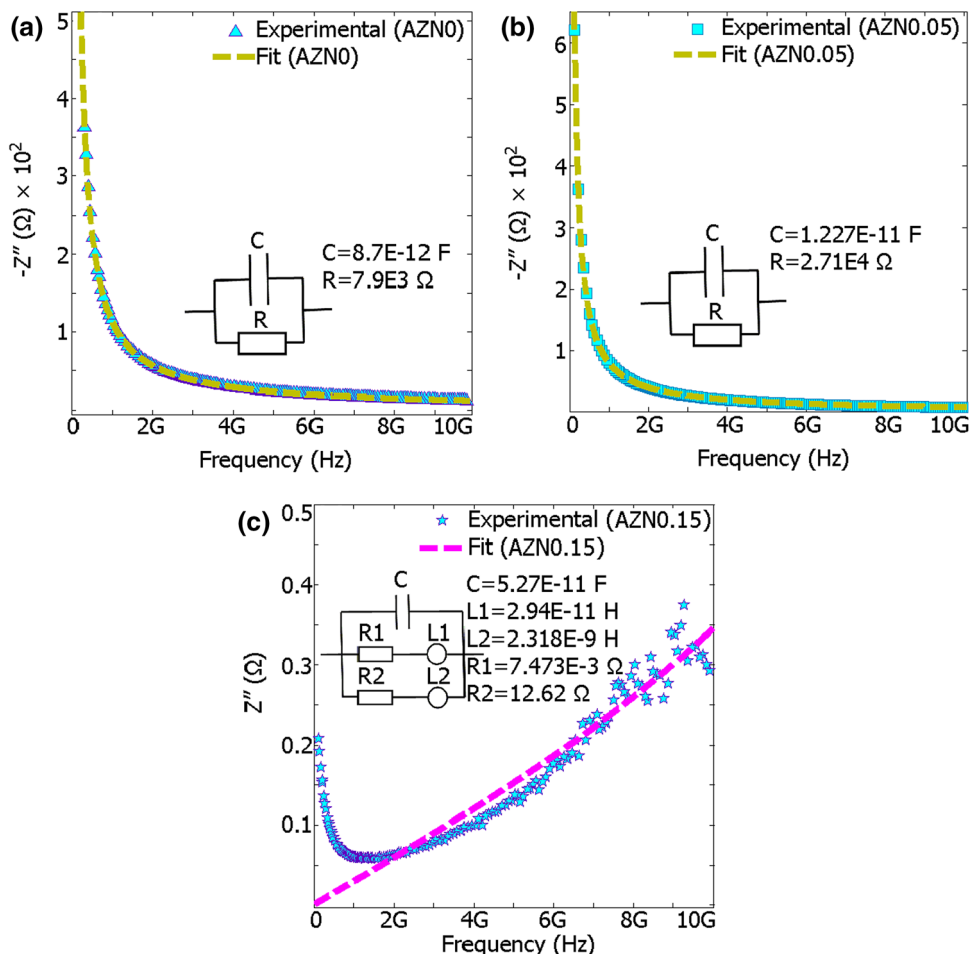
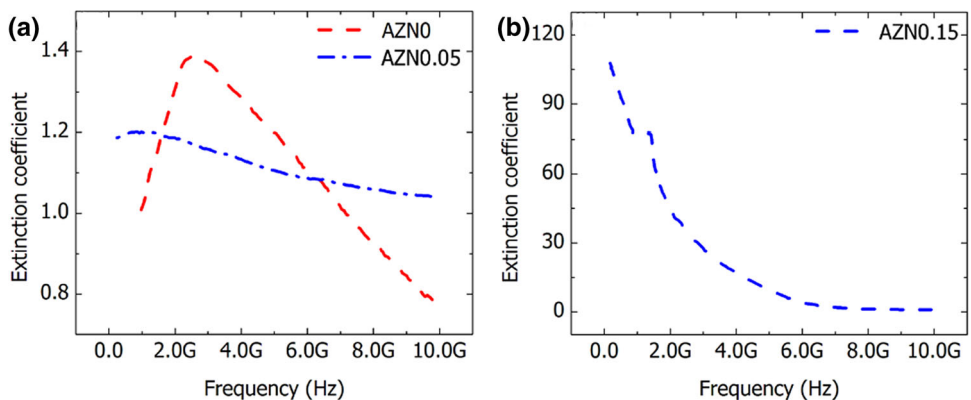


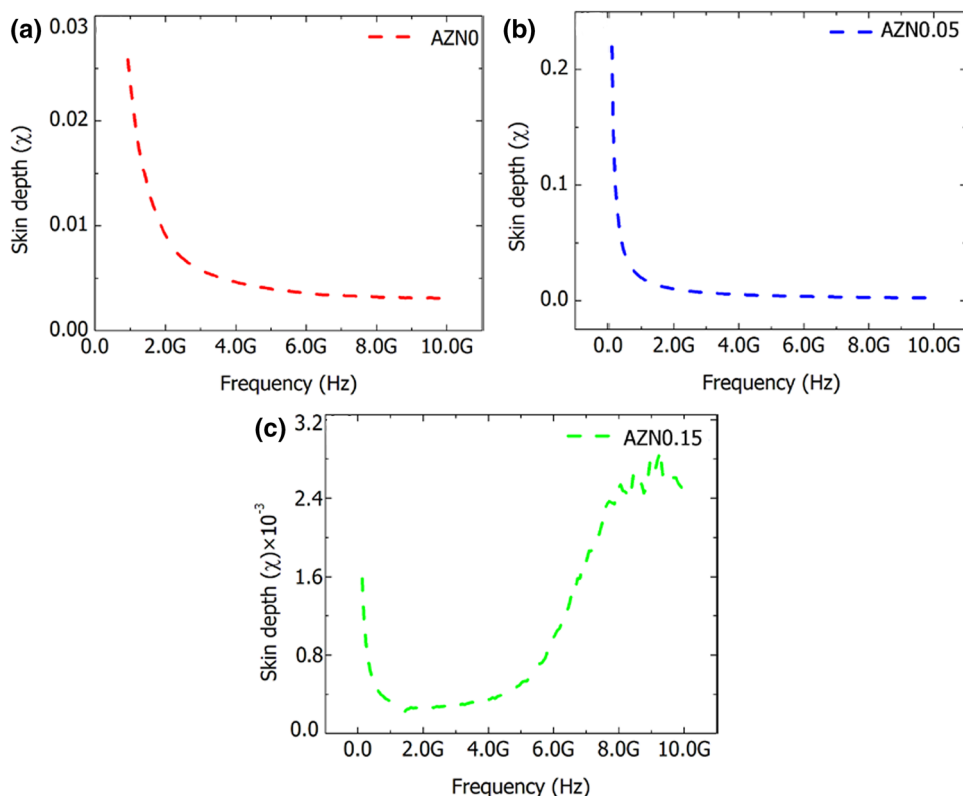
Fig. 13 Extinction coefficient of AZN_x samples **a** $x = 0$ and 0.05 ; **b** $x = 0.15$



As shown in Fig. 12a, b, AZN0 and AZN0.05 samples can be simulated by an equivalent circuit model composed of a parallel combination of resistor R and capacitor C . We can see that, with the increase of silver content, R decreases due to the enhanced leakage conductance and C increases due to the increase of Ag-Zr_{0.9}Ni_{0.1}O_y interface area. For AZN0.15, shunt inductors

are introduced into the equivalent circuit models (Fig. 12c). In composite right-/left-handed transmission line metamaterials, negative ϵ'_e is usually provided by shunt inductances. The negative ϵ'_e of AZN0.15 sample could be ascribed to its shunt inductances, which are caused by the current loops in interconnected silver particles (above p_c).

Fig. 14 The variation of skin depth with frequency for AZNx samples **a** AZN0; **b** AZN0.05; **c** AZN0.15



3.6 Extinction coefficient and skin depth spectra

Figure 13 shows extinction coefficient (imaginary part of the effective refractive index) of AZNx samples calculated by formula as follows:

$$k = \frac{\mu_e''\epsilon_e' + \mu_e'\epsilon_e''}{\sqrt{2}(|\epsilon_e||\mu_e| + \mu_e'\epsilon_e' - \mu_e''\epsilon_e'')}^{1/2} \tag{7}$$

It was also found that as the molar silver content increased to 0.05, the intensity of the peak became weaker and broader. Moreover, the shift of peak toward the lower frequency is observed when the Ag content increases. The extinction coefficient for AZN0.15 decreases with increasing frequency, because ϵ_e' becomes negative giving rise to a practically imaginary refractive index. After making of the nanowire structure, the intrinsic optical transition has a shift to the low-energy range, which means that the band gaps are narrowed by Ag atoms.

It observes that the extinction coefficient increases for AZN0.15 than that of AZN0 and AZN0.05. For AZN0.15 sample, extinction coefficient decreases sharply to frequency 3 GHz and then decreases gradually to frequency 10 GHz. In general, the extinction coefficient values increase with increasing doping above p_c .

The skin depth (χ) is a measure of the penetration of a plane electromagnetic wave into a material. The skin depth of AZNx samples calculated by formula as follows:

$$\chi = \frac{c}{4\pi n''\nu} \tag{8}$$

where c is speed of light in vacuum and n'' is imaginary part of the effective refractive index. Figure 14 represents the plot of skin depth versus wavelength. As Fig. 14a, b shows, the skin depth decreases with increasing frequency below p_c . For AZN0.15 sample (above p_c), it is observed that value of skin depth decreases with frequency to 1 GHz and then increases.

4 Conclusions

We have discussed the preparation process and the morphological, electrical, magnetical, and optical properties of Ag/Zr_{0.9}Ni_{0.1}O_y nanocomposites at microwave frequencies. The effective properties of this nanocomposite have been shown to be useful for DNMs at this range of frequencies. We discussed the dependency of effective properties on the material from which the nanocomposites are made. We found that the PVP molecules play a key role in the formation of a wired-like network structure of Ag and mainly act as the structure-directing agent of Ag. The shape of Ag nanoparticles is also controllable by changing the atomic ratios. Our results may be very helpful to better understand the dielectric properties of nanocomposites in microwave frequency region and optimize device parameters in the

future. The stronger intrinsic absorption of good metals such as Au and Ag eventually turns out to be something useful, since it suppresses the interaction between neighboring nanoparticles in the nanocomposite. The outcome is negative ϵ'_c and μ'_c for AZN0.15. The tunability of negative permittivity and permeability makes AZN0.15 as a promising candidate for the DNMs.

References

1. S. Tanabe, Y. Nakagawa, T. Okamoto, M. Haraguchi, T. Isu, G. Shinomiya, Erratum to: fabrication and evaluation of photonic metamaterial crystal. *Appl. Phys. A* **112**, 613 (2013)
2. R. Gholipur, A. Bahari, Random nanocomposites as metamaterials: preparation and investigations at microwave region. *Opt. Mater.* **50**, 175 (2015)
3. W. Zhu, X. Zhao, B. Gong, L. Liu, B. Su, Optical metamaterial absorber based on leaf-shaped cells. *Appl. Phys. A* **112**, 147 (2010)
4. S. Linden, C. Enkrich, M. Wegener, J.F. Zhou, T. Koschny, C.M. Soukoulis, Magnetic response of metamaterials at 100 terahertz. *Science* **306**, 1351 (2004)
5. W.S. Cai, U.K. Chettiar, H.K. Yuan, V.C. de Silva, A.V. Kildishev, V.P. Drachev, V.M. Shalaev, Metamagnetics with rainbow colors. *Opt. Express* **15**, 3333 (2007)
6. V.M. Shalaev, W.S. Cai, U.K. Chettiar, H.K. Yuan, A.K. Sarychev, V.P. Drachev, A.V. Kildishev, Negative index of refraction in optical metamaterials. *Opt. Lett.* **30**, 3356 (2005)
7. S. Zhang, W.J. Fan, N.C. Panoiu, K.J. Malloy, R.M. Osgood, S.R.J. Brueck, Experimental demonstration of near-infrared negative-index metamaterials. *Phys. Rev. Lett.* **95**, 137404 (2005)
8. G. Dolling, C. Enkrich, M. Wegener, C.M. Soukoulis, S. Linden, Simultaneous negative phase and group velocity of light in a metamaterial. *Science* **312**, 892 (2006)
9. G. Dolling, M. Wegener, C.M. Soukoulis, S. Linden, Negative-index metamaterial at 780 nm wavelength. *Opt. Lett.* **32**, 53 (2007)
10. U.K. Chettiar, A.V. Kildishev, H.K. Yuan, W.S. Cai, S.M. Xiao, V.P. Drachev, V.M. Shalaev, Dual-band negative index metamaterial: double negative at 813 nm and single negative at 772 nm. *Opt. Lett.* **32**, 1671 (2007)
11. E. Plum, V.A. Fedotov, A.S. Schwanecke, N.I. Zheludev, Y. Chen, Giant optical gyrotropy due to electromagnetic coupling. *Appl. Phys. Lett.* **90**, 223113 (2007)
12. M. Decker, M.W. Klein, M. Wegener, S. Linden, Circular dichroism of planar chiral magnetic metamaterials. *Opt. Lett.* **32**, 856 (2007)
13. M.W. Klein, C. Enkrich, M. Wegener, S. Linden, Second-harmonic generation from magnetic metamaterials. *Science* **313**, 502 (2006)
14. M.W. Klein, M. Wegener, N. Feth, S. Linden, Experiments on second- and third harmonic generation from magnetic metamaterials. *Opt. Express* **15**, 5238 (2007)
15. A.K. Popov, V.M. Shalaev, Negative-index metamaterials: second-harmonic generation, Manley-Rowe relations and parametric amplification. *Appl. Phys. B* **84**, 131 (2006)
16. A.K. Popov, V.M. Shalaev, Compensating losses in negative-index metamaterials by optical parametric amplification. *Opt. Lett.* **31**, 2169 (2006)
17. N. Fang, H. Lee, C. Sun, X. Zhang, Sub-diffraction-limited optical imaging with a silver superlens. *Science* **308**, 534 (2005)
18. T. Taubner, D. Korobkin, Y. Urzhumov, G. Shvets, R. Hillenbrand, Near-field microscopy through a SiC superlens. *Science* **313**, 1595 (2006)
19. Z.W. Liu, H. Lee, Y. Xiong, C. Sun, X. Zhang, Far-field optical hyperlens magnifying subdiffraction-limited objects. *Science* **315**, 1686 (2007)
20. Z.W. Liu, S. Durant, H. Lee, Y. Pikus, N. Fang, Y. Xiong, C. Sun, X. Zhang, Far-field optical superlens. *Nano Lett.* **7**, 403 (2007)
21. W.S. Cai, D.A. Genov, V.M. Shalaev, Superlens based on metal-dielectric composites. *Phys. Rev. B* **72**, 193101 (2005)
22. Z. Jacob, L.V. Alekseyev, E. Narimanov, Optical hyperlens: far-field imaging beyond the diffraction limit. *Opt. Express* **14**, 8247 (2006)
23. J.B. Pendry, D. Schurig, D.R. Smith, Controlling electromagnetic fields. *Science* **312**, 1780 (2006)
24. D. Schurig, J.J. Mock, B.J. Justice, S.A. Cummer, J.B. Pendry, A.F. Starr, D.R. Smith, Metamaterial electromagnetic cloak at microwave frequencies. *Science* **314**, 977 (2006)
25. W.S. Cai, U.K. Chettiar, A.V. Kildishev, V.M. Shalaev, Optical cloaking with metamaterials. *Nat. Photonics* **1**, 224 (2007)
26. W.S. Cai, U.K. Chettiar, A.V. Kildishev, V.M. Shalaev, G.W. Milton, Nonmagnetic cloak with minimized scattering. *Appl. Phys. Lett.* **91**, 111105 (2007)
27. W.S. Cai, U.K. Chettiar, A.V. Kildishev, V.M. Shalaev, Designs for optical cloaking with high-order transformations. *Opt. Express* **16**, 5444 (2008)
28. J.B. Pendry, A.J. Holden, W.J. Stewart, I. Youngs, Extremely low frequency plasmons in metallic structures. *Phys. Rev. Lett.* **76**, 4773 (1996)
29. J.B. Pendry, A.J. Holden, D.J. Robbins, W.J. Stewart, Magnetism from conductors and enhanced nonlinear phenomena. *IEEE Trans. Microw. Theory Tech.* **47**, 2075 (1999)
30. J.B. Pendry, L. Martin-Moreno, F.J. Garcia-Vidal, Mimicking surface plasmons with structured surfaces. *Science* **305**, 847 (2004)
31. A.V. Krasavin, K.F. MacDonald, A.S. Schwanecke, N.I. Zheludev, Gallium/aluminum nanocomposite material for nonlinear optics and nonlinear plasmonics. *Appl. Phys. Lett.* **89**, 031118 (2006)
32. T. Kume, T. Amano, S. Hayashi, K. Yamamoto, Attenuated total reflection spectroscopy of Ag-SiO₂ composite films. *Thin Solid Films* **264**, 115 (1995)
33. A.K. Sarychev, V.M. Shalaev, Electromagnetic field fluctuations and optical nonlinearities in metal-dielectric composites. *Phys. Rep.* **335**, 276 (2000)
34. V.A. Shubin, A.K. Sarychev, J.P. Clerc, V.M. Shalaev, Local electric and magnetic fields in semicontinuous metal films: beyond the quasistatic approximation. *Phys. Rev. B* **62**, 11230 (2000)
35. W. Cai, V. Shalaev, *Optical Metamaterials: Fundamentals and Applications* (Springer, New York, 2009)
36. V.M. Shalaev, A.K. Sarychev, Nonlinear optics of random metal-dielectric films. *Phys. Rev. B* **57**, 13265 (1998)
37. A.K. Sarychev, V.A. Shubin, V.M. Shalaev, Anderson localization of surface plasmons and nonlinear optics of metal-dielectric composites. *Phys. Rev. B* **60**, 16389 (1999)
38. D.J. Bergman, D. Stroud, Physical properties of macroscopically inhomogeneous media. *Solid State Phys.* **46**, 147 (1992)
39. M.D. Thoreson, J. Fang, A.V. Kildishev, L.J. Prokopeva, P. Nyga, U.K. Chettiar, V.M. Shalaev, V.P. Drachev, Fabrication and realistic modeling of three-dimensional metal-dielectric composites. *J. Nanophotonics* **5**, 051513 (2011)
40. T. Tsutaoka, T. Kasagi, S. Yamamoto, K. Hatakeyama, Low frequency plasmonic state and negative permittivity spectra of

- coagulated Cu granular composite materials in the percolation threshold. *Appl. Phys. Lett.* **102**, 181904 (2013)
41. L. Shi, L. Gao, S. He, B. Li, Superlens from metal-dielectric composites of nonspherical particles. *Phys. Rev. B* **76**, 045116 (2007)
 42. X. Li, F. Zhuang, Multilayered structures with high subwavelength resolution based on the metal-dielectric composites. *J. Opt. Soc. Am. A*: **26**, 2521 (2009)
 43. L. Shi, L. Gao, Subwavelength imaging from a multilayered structure containing interleaved nonspherical metal-dielectric composites. *Phys. Rev. B* **77**, 195121 (2008)
 44. Y. Xiong, Z.W. Liu, S. Durant, H. Lee, C. Sun, X. Zhang, Tuning the far-field superlens: from UV to visible. *Opt. Express* **15**, 7095 (2007)
 45. U.K. Chettiar, A.V. Kildishev, T.A. Klar, V.M. Shalaev, Negative index metamaterial combining magnetic resonators with metal films. *Opt. Express* **14**, 7872 (2006)
 46. L. Menon, W.T. Lu, A.L. Friedman, S.P. Bennett, D. Heiman, S. Sridhar, Negative index metamaterials based on metal-dielectric nanocomposites for imaging applications. *Appl. Phys. Lett.* **93**, 123117 (2008)
 47. J.S. Parramon, V. Janicki, H. Zorc, On the dielectric function tuning of random metal-dielectric nanocomposites for metamaterial applications. *Opt. Express* **18**, 26915 (2010)
 48. V.M. Shalaev, A.K. Sarychev, Nonlinear optics of random metal-dielectric films. *Phys. Rev. B* **57**(20), 13265 (1998)
 49. S. Arslanagić, T.V. Hansen, N.A. Mortensen, A.H. Gregersen, O. Sigmund, R.W. Ziolkowski, O. Breinbjerg, A review of the scattering-parameter extraction method with clarification of ambiguity issues in relation to metamaterial homogenization. *IEEE Antennas Propag. Mag.* **55**(2), 91–106 (2013)
 50. K.L. Yan, R.H. Fan, Z.C. Shi, M. Chen, L. Qian, Y.L. Wei, K. Sun, J. Li, Negative permittivity behavior and magnetic performance of perovskite $\text{La}_{1-x}\text{Sr}_x\text{MnO}_3$ at high-frequency. *J. Mater. Chem. C* **2**, 1028 (2014)
 51. G.E.M. Jauncey, F. Pennell, Scattering of X-rays from powdered crystals. *Phys. Rev. B* **43**, 505 (1933)